Chemical Science

ROYAL SOCIETY OF CHEMISTRY

EDGE ARTICLE

View Article Online
View Journal

Cite this: DOI: 10.1039/d6sc02262f

All publication charges for this article have been paid for by the Royal Society of Chemistry

Cascade charge-transport-chain engineering in alloy nanocluster–semiconductor artificial photosystems

Zi-Han Zheng,[a] Qing Chen,[a] Peng Su,[a] Lifeng Cai,*[b] Jie Liang,[b] Guangcan Xiao[c] and Fang-Xing Xiao *[a]

Received 19th March 2026
Accepted 22nd April 2026

DOI: 10.1039/d6sc02262f

rsc.li/chemical-science

Atomically precise metal nanoclusters (NCs), featuring a discrete electronic structure and pronounced quantum confinement effects, are emerging as promising photosensitizers for artificial photosystems; however, their practical implementation remains fundamentally constrained by rapid charge recombination and poorly controlled charge transport. Here, we introduce a conceptual cascade charge-transport-chain engineering strategy that addresses this intrinsic bottleneck by constructing directional and continuous carrier transport pathways across NC–semiconductor interfaces. By integrating alloy NC photosensitization with atomic Ni doping of TiO_2, robust interfacial electronic coupling is established, enabling directional and accelerated extraction of photogenerated carriers. The resulting BNC/Ni–TiO_2 heterostructures exhibit markedly enhanced visible-light-driven hydrogen evolution, accompanied by effective suppression of charge recombination within alloy NCs. Combined experimental and theoretical investigations reveal that the performance enhancement originates from cascade charge-transport-chain engineering rather than simple binary synergy. This work provides a general design principle for constructing tunable charge-transport pathways with alloy NCs, advancing NC-based artificial photosystems toward solar-to-hydrogen energy conversion.

1. Introduction

Atomically precise nanoclusters (NCs) with discrete electronic structures and pronounced quantum confinement effects, have emerged as promising photosensitizers for artificial photosystems, owing to their superior light-harvesting properties.[1,2] However, the widespread application of metal NCs is hindered by fundamental challenges, such as rapid charge recombination and poorly controlled charge transport, which prevent the construction of stable and efficient metal NC-based systems.[3]

In recent years, heterometallic NCs particularly bimetallic NCs (BNCs) have garnered increasing attention as a new generation of light-harvesting antennae for solar energy conversion. BNCs are synthesized by incorporating two different metals into a single nanocluster unit, offer a promising strategy to overcome the inherent limitations of traditional monometallic NCs through bimetallic synergy. Through atomic-scale manipulation of metal composition and spatial arrangement, BNCs offer distinct advantages, including (i) precise control of their geometric and electronic structures; (ii) enhanced light-harvesting efficiency, and (iii) accelerated charge transport kinetics. These features position BNCs as ideal active centers for photon capture and catalytic reactions.[4] Despite these compelling merits, the use of BNCs as photocatalysts remains limited by poor charge separation efficiency and low photocatalytic activity. To address these challenges, one promising strategy is the coupling of BNCs with metal oxide semiconductors, such as titanium dioxide (TiO_2), to form heterostructures with optimized energy level alignment. This integration extends the photo-response range of the metal oxide substrate and enhances charge migration and separation over the BNCs, facilitating efficient photoredox catalysis. However, achieving efficient charge transport and separation remains a critical issue in the design of high-performance artificial photosystems.

A promising solution lies in the deposition of suitable co-catalysts (*e.g.*, Ru, Pd, and Pt) on the TiO_2 surface, which increases the number of active sites for accelerated photocatalytic reactions while mitigating carrier recombination.[5] Among these co-catalysts, nickel (Ni) stands out as a low-cost and efficient option for photocatalytic hydrogen generation due to its ability to boost charge transfer kinetics and its strong affinity for active hydrogen species.[6] Combining Ni with BNCs offers a dual-functional strategy for increasing the number of active sites on TiO_2 and extending the visible light absorption

[a]College of Materials Science and Engineering, Fuzhou University, New Campus, Fujian, 350116, P. R. China. E-mail: fxxiao@fzu.edu.cn

[b]College of Environmental and Biological Engineering, Fujian Provincial Key Laboratory of Ecology-Toxicological Effects & Control for Emerging Contaminants, Putian University, Putian, Fujian, 351100, P. R. China. E-mail: 89437499@qq.com

[c]Instrumental Measurement and Analysis Center, Fuzhou University, Fuzhou, 350108, P.R. China

capabilities of TiO_2, which together maximize solar energy utilization and drive charge flow.[6b,7] By strategically incorporating Ni co-catalysts and simultaneously anchoring alloy NCs ($Au_{1-x}Ag_x$, $Au_{1-x}Pt_x$, and $Au_{1-x}Cu_x$) onto TiO_2, and fine-tuning the interface configuration, we hypothesize that a controllable charge transport pathway can be stimulated. Once the appropriate energy level alignment between the components is optimized, this will facilitate accelerated directional charge migration and suppress carrier recombination, ultimately leading to significantly improved photocatalytic hydrogen production performance under visible light. This integrated strategy paves the way for the development of novel alloy NC-based artificial photosystems.

Inspired by these insights, herein, we conceptually present a cascade charge-transport-chain engineering strategy *via* constructing TiO_2–Ni/BNC ($Au_{1-x}Ag_x$, $Au_{1-x}Pt_x$, and $Au_{1-x}Cu_x$) heterostructure artificial photosystems for solar-to-hydrogen conversion. Specifically, Ni is doped onto the surface of TiO_2 nanosheets *via* a molten-salt method (MSM), followed by electrostatic self-assembly of tailor-made alloy NCs onto the Ni-doped TiO_2 (TiO_2–Ni) to form the TiO_2–Ni/BNC ($Au_{1-x}Ag_x$, $Au_{1-x}Pt_x$, and $Au_{1-x}Cu_x$) ternary photocatalysts. The results demonstrate that the photosensitization effect of BNCs broadens the light absorption range of pristine TiO_2, while the accelerated interfacial charge transfer enabled by Ni doping significantly enhances the photocatalytic hydrogen evolution activities of the TiO_2–Ni/BNC heterostructures under visible light. Through a combination of experimental and theoretical investigations, we elucidate the charge transfer mechanism within the TiO_2–Ni/BNC photosystems, revealing a synergistic effect between atomic-scale BNCs and metal oxide supports. This work highlights the promising potential of BNCs as high-performance photosensitizers and presents a novel approach to engineering cascade charge-transport-chains that enhance the efficiency of metal NC–semiconductor hybrid artificial photosystems for efficient solar-to-hydrogen energy conversion.

2. Experimental section

2.1 Materials

All the materials were of analytical grade and used as received without further purification, and the detailed information is provided in the SI.

2.2 Preparation of photocatalysts

2.2.1 Preparation of TiO_2 nanosheets. Under vigorous stirring, 4.9 mL of 40 wt% hydrofluoric acid (HF) solution was dropped into 50 mL of tetrabutyl titanate (TBOT) in a 100 mL Teflon-lined stainless steel autoclave. The mixture was heated in an electric oven at 180 °C for 24 h to get a white powder. The separated solid was successively washed with ethanol, 0.1 M NaOH, and deionized water to obtain the TiO_2 nanosheets.[8]

2.2.2 Preparation of TiO_2–Ni nanocomposites. TiO_2–Ni is prepared by a modified molten-salt method. In a typical process, 10 mg of $NiCl_2 \cdot 6H_2O$, 0.9 g of LiCl, 1.1 g of KCl and 1 g of TiO_2 nanosheets are pestled in a mortar for 0.5 h to obtain a uniform mixture, which is then transferred into a semi-capped corundum crucible. Next, the crucible is put into a tube furnace and calcined at 773 K for 2 h under a N_2 atmosphere (heating rate: 8 K min^{-1}). After cooling down to 298 K naturally, the mixture is washed thoroughly with deionized water five times to remove the salt (LiCl & KCl) and then the thus-obtained TiO_2–$Ni_{0.25}$ is dried in a vacuum oven at 333 K.[9] In addition, the loading amount of Ni is tuned by adding 5, 10, 20, and 40 mg of $NiCl_2 \cdot 6H_2O$ in the recipe, and the mixtures are labeled TiO_2–Ni_m ($m = 0.12$, 0.25, 0.46, 0.93).

2.2.3 Preparation of bimetallic NCs. $Au_{1-x}Ag_x$ NCs were synthesized according to a previous study with some modifications.[10] Aqueous solutions of $HAuCl_4$ (20 mM, 0.50 mL), $AgNO_3$ (20 mM, 0.10 mL) and GSH (100 mM, 0.15 mL) were mixed with 4.35 mL of deionized water at 25 °C. The reaction mixture was heated to 70 °C under gentle stirring (1000 rpm) for 24 h in air. Then $Au_{1-x}Ag_x$ NCs were cooled down to room temperature to obtain a yellow solution, which was stored in a refrigerator at 4 °C for further use. The fabrication of $Au_{1-x}Cu_x$ NCs and $Au_{1-x}Pt_x$ NCs is akin to that of the $Au_{1-x}Ag_x$ NCs by replacing $AgNO_3$ with $Cu(NO_3)_2$ and chloroplatinic acid hexahydrate ($H_2PtCl_6 \cdot 6H_2O$), respectively.

2.2.4 Preparation of TiO_2–Ni/BNC heterostructures. 0.1 g TiO_2-Ni_m was dispersed into $Au_{1-x}Ag_x$ NCs aqueous solution under vigorous stirring (1000 rpm) for 1 h. Pre-set X mL ($X = 5$, 7, 10, 13, 15) of $Au_{1-x}Ag_x$ NC aqueous solution was diluted to different concentrations with deionized water. The reaction mixture was centrifuged, then washed with ethanol and deionized water and dried in a vacuum at 60 °C for 8 h. The mixtures were labeled TiO_2-Ni_m/$n$$Au_{1-x}Ag_x$ ($n = 5$, 7, 10, 13, 15). When the photocatalyst contains 0.25 wt% Ni and 10 mL of $Au_{1-x}Ag_x$ NCs, it represents the optimal sample for the subsequent systematic investigation and is defined as T-$Ni_{0.25}$/$Au_{1-x}Ag_x$. Similarly, the preparation of TiO_2–$Ni_{0.25}$/$Au_{1-x}Cu_x$ and TiO_2–$Ni_{0.25}$/$Au_{1-x}Pt_x$ followed the same procedure as that for T-$Ni_{0.25}$/$Au_{1-x}Ag_x$, using 10 mL of $Au_{1-x}Cu_x$ and $Au_{1-x}Pt_x$ precursor solutions, respectively, in place of $Au_{1-x}Ag_x$.

2.3 Characterization

The crystal structure was determined by X-ray diffraction (XRD, Miniflex600). Morphologies were visualized by field emission scanning electron microscopy (FESEM, Supra55, Carl Zeiss) equipped with energy-dispersive spectroscopy (EDS) and transmission electron microscopy (TEM, Tecnai G2 F20). Fourier transform infrared (FTIR) spectra were recorded on an infrared spectrophotometer (TJ270-30A). Raman spectra were collected with a Raman spectrometer (Dxr-2xi, Thermo Scientific, America). UV-visible diffuse reflectance spectra (DRS) were measured on a Cary50 (Varian, America) with a reflectance background of 200 to 800 nm. X-ray photoelectron spectra (XPS) were recorded on a photoelectron spectrometer (ESCALAB 250, Thermo Scientific, America), and the binding energy (BE) of the elements was calibrated by the BE of C 1s (284.80 eV). Zeta potential (ξ) measurements were performed by dynamic light scattering analysis (Zeta sizer Nano ZS-90). Time-resolved photoluminescence (TRPL) spectra were measured on a FLS 920

fluorescence lifetime spectrophotometer (Edinburgh, Instruments, UK). The photoluminescence (PL) spectra were probed on a Varian Cary Eclipse spectrophotometer. Brunauer–Emmett–Teller (BET) specific surface area and N_2 adsorption experiments were performed on an ASAP 2460. Concentrations of T-$N_{0.25}$/10$Au_{1-x}Ag_x$ were quantified by inductively coupled plasma emission spectroscopy (ICP, XSERIES 2 ICP-MS). X-ray absorption fine structure (XAFS) spectroscopy was carried out using a Rapid XAFS 2M (Anhui Absorption Spectroscopy Analysis Instrument Co., Ltd) in transmission (or fluorescence) mode at 20 kV and 30 mA. Kelvin-Probe Force Microscopy (KPFM) was performed on a Dimension Icon (Bruker, America).

2.4 Photocatalytic H_2 production performances

Photocatalytic reactions were conducted on an online photocatalytic hydrogen production system using a Pyrex vessel. Specifically, 10 mg of the catalyst was dispersed in mixed solution (DI H_2O, 2 mL), and then triethanolamine (TEOA, 0.5 mL) was added as the sacrificial agent. The photocatalytic system was thoroughly degassed and irradiated with a 300 W Xe lamp (PLS-SXE300D, Beijing Perfectlight Technology Co., Ltd) equipped with a 420 nm-cut-off optical filter (λ > 420 nm). Continuous magnetic stirring was applied at the bottom of the reactor to keep the catalyst in suspension during the whole experiment. The evolved H_2 was monitored periodically using an online gas chromatograph (Shimadzu GC-8A with an MS-5A column using argon as carrier gas). Photoactivities were evaluated based on the H_2 evolution amount in the first 2 h of the reaction. Cyclic photocatalytic H_2 evolution reactions were carried out as follows. Specifically, the photocatalytic system was thoroughly degassed again after the first run without separating the catalysts and supplementing the TEOA. Subsequently, the thoroughly degassed system was irradiated again with a 300 W Xe lamp S10 with a UV-CUT filter to cut off light with a wavelength λ < 420 nm. Analogously, the following four runs of photocatalytic recycling tests were performed.

2.5 Photoelectrochemical (PEC) measurements

PEC measurements were carried out on an electrochemical workstation (CHI660E, CHI Shanghai, Inc.) under visible light irradiation (λ > 420 nm) (PLS-SXE300D, Beijing Perfect Light Co. Ltd, China), with a conventional three-electrode system and 0.5 M Na_2SO_4 aqueous solution (pH = 6.69) was utilized as the electrolyte. The three-electrode system is composed of Pt foil (1 cm × 1 cm) as the counter electrode, an Ag/AgCl electrode as the reference electrode, and working electrodes. The working electrodes were prepared on fluorine-doped tin oxide (FTO) glass that was cleaned by sonication in DI H_2O and ethanol for 30 min and dried at 60 °C in an oven. The specific operational information is provided in the SI.

3. Results and discussion

3.1 Structural characterization

The synthesis procedures of the TiO_2–$Ni_{0.25}$/$Au_{1-x}Ag_x$ ternary heterostructure are depicted in Scheme 1. Initially, the Ni element was doped on the TiO_2 nanosheets by MSM. Upon reaching the melting point of 625 K, the salts form a liquid phase, $NiCl_2$ dissolves and is dispersed, generating a strong polarizing force (a pool of ionized anions and cations).[11] This force destabilizes the Ti–O bonds on the surface of TiO_2 nanosheets, facilitating the formation of Ni–O bonds between surface oxygen ions and mobile Ni^{2+} ions. Furthermore, inserting Ni^{2+} ions into the pre-formed, tightly bonded TiO_2 lattice would require overcoming both lattice distortion energy and high diffusion energy barriers, which is thermodynamically unfavorable.[12] Therefore, the MSM promotes the formation of stable Ni–O bonds on the TiO_2 surface at relatively low temperature, thereby effectively preserving the structural integrity of the TiO_2 structures. Subsequently, $Au_{1-x}Ag_x$ NCs were deposited onto the Ni-doped TiO_2 (TiO_2–Ni) through electrostatic self-assembly under ambient conditions, resulting in the TiO_2–Ni/$Au_{1-x}Ag_x$ ternary heterostructures. More specifically, under acidic conditions, abundant hydroxyl (–OH) groups on the surface of TiO_2 facilitate the proton (H^+) migration and adsorption, rendering the surface positively charged.[13] The surface of $Au_{1-x}Ag_x$ NCs (*ca.* 1.7 nm) is capped with glutathione (GSH) ligands bearing carboxyl ($-COO^-$) functional groups, and thus they feature a negatively charged surface (Fig. S1). Thus, negatively charged $Au_{1-x}Ag_x$ NCs are attracted by the positively charged TiO_2 substrate *via* electrostatic interaction, ultimately

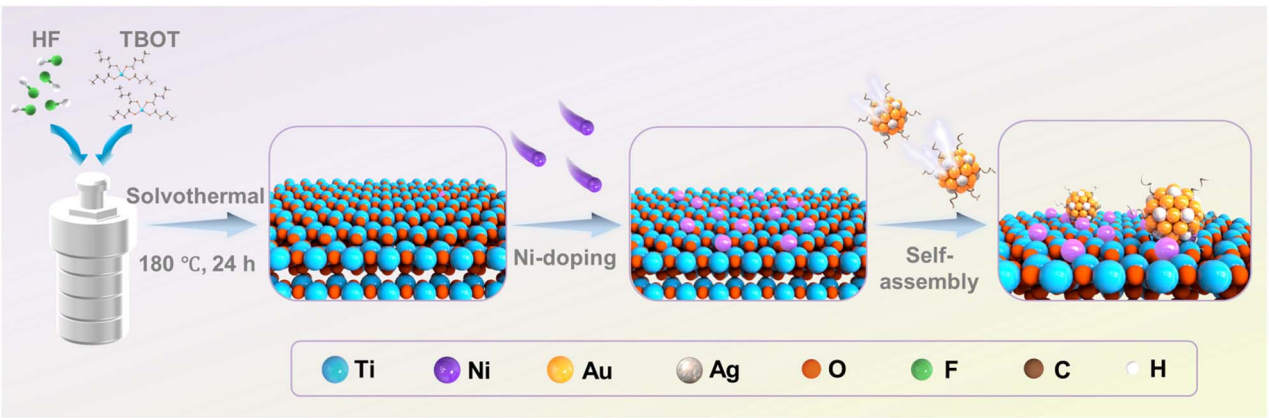

Scheme 1 Schematic flowchart depicting the fabrication of TiO_2–$Ni_{0.25}$/$Au_{1-x}Ag_x$ heterostructures.

forming the $TiO_2/Au_{1-x}Ag_x$ NCs heterostructure under ambient conditions. Similarly, Ni-doped TiO_2 assembles with the $Au_{1-x}Ag_x$ NCs in the same way, giving rise to the TiO_2–Ni/$Au_{1-x}Ag_x$ NCs heterostructure. After Ni doping and $Au_{1-x}Ag_x$ NC decoration, the color of the samples gradually changes from white to yellow (Fig. S2), indicating the successful modification of TiO_2. This electrostatic self-assembly strategy is also utilized to fabricate the TiO_2–Ni/alloy NC ($Au_{1-x}Pt_x$ and $Au_{1-x}Cu_x$) ternary heterostructures. The detailed characterization of $Au_{1-x}Cu_x$ and $Au_{1-x}Pt_x$ NCs is specifically illustrated in Fig. S3 and S4, respectively.

As shown in Fig. 1a, all the XRD results of TiO_2, T-$Ni_{0.25}$, T/$Au_{1-x}Ag_x$, and T-$Ni_{0.25}$/$Au_{1-x}Ag_x$ exhibit the characteristic diffraction peaks at 25.3°, 37.8°, and 48.0°, corresponding to the (101), (004), and (200) crystal planes of anatase TiO_2 (JCPDS: 99-0008), respectively.[8] This observation confirms that Ni doping and $Au_{1-x}Ag_x$ NC loading preserve the crystalline phase of TiO_2. The absence of distinct diffraction peaks of $Au_{1-x}Ag_x$ NCs or metallic Ni species can be attributed to their low content and high dispersion in the nanocomposite. Raman results (Fig. S5) further corroborate the anatase phase of TiO_2, with no observable signals for $Au_{1-x}Ag_x$ NCs or Ni dopant, aligning with the XRD results. It should be emphasized that the significant enhancement of the E_g peak intensity observed after Ni doping can be attributed to a surface-enhanced resonance Raman scattering (SERRS) effect.[2a,14]

Fourier transform infrared (FTIR) spectroscopy (Fig. 1b and Table S1) results of all the samples reveal an apparent peak at 1390 cm^{-1}, which is assigned to the Ti–O vibrational modes.[15] Particularly, T/$Au_{1-x}Ag_x$ and T-$Ni_{0.25}$/$Au_{1-x}Ag_x$ exhibit additional peaks at 1640, 1530, 3241, and 2925 cm^{-1}, corresponding to the C=O, N–H, and C–H functional groups derived from the GSH ligands stabilizing the $Au_{1-x}Ag_x$ NCs.[16] These features strongly confirm the successful deposition of $Au_{1-x}Ag_x$ NCs on the TiO_2 substrate.

Diffuse reflectance spectroscopy (DRS) results (Fig. 1c and d) demonstrate that the incorporation of $Au_{1-x}Ag_x$ NCs and Ni doping significantly enhance the visible-light harvesting

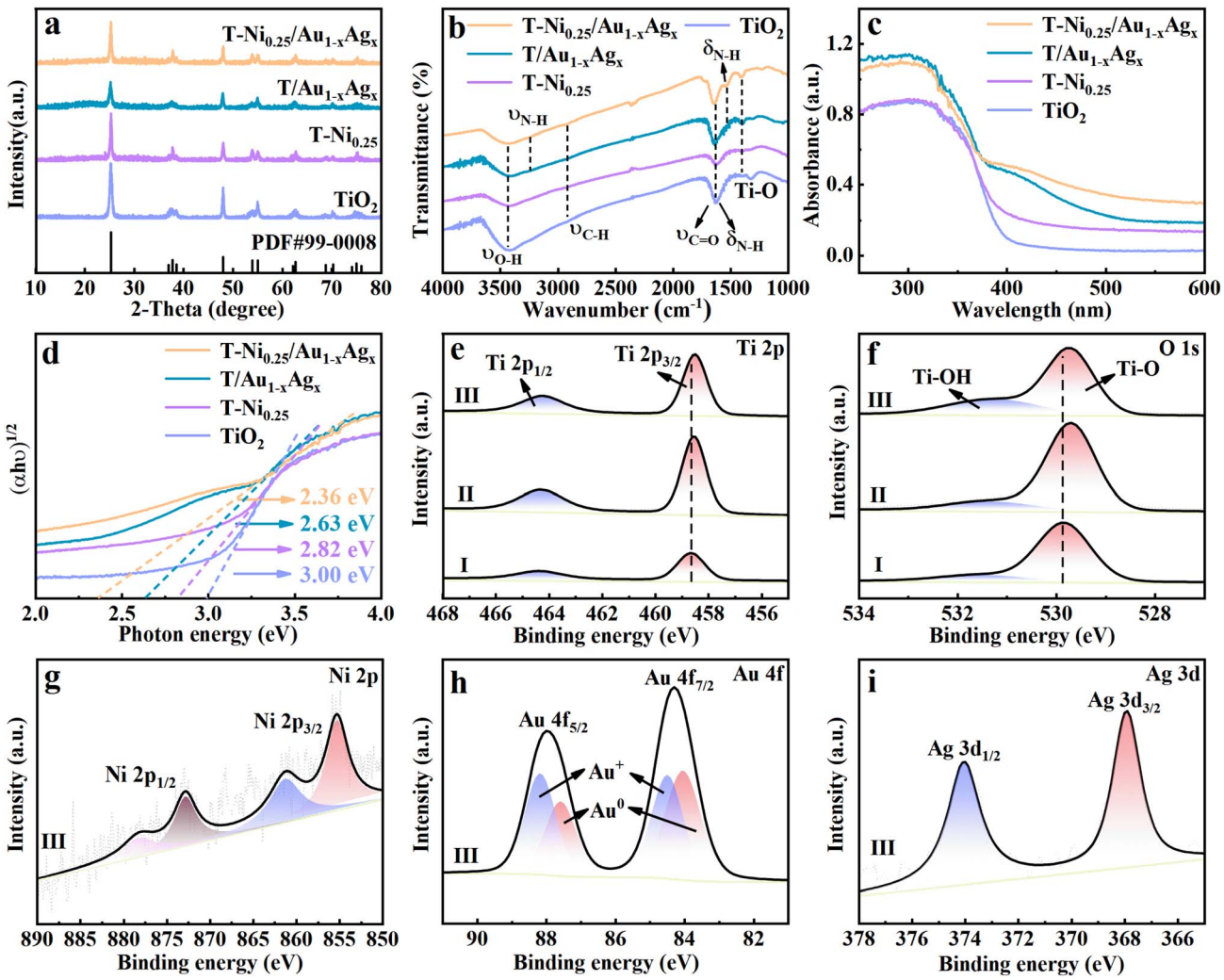

Fig. 1 (a) XRD patterns and (b) FTIR spectra of pristine TiO_2, T-$Ni_{0.25}$, T/$Au_{1-x}Ag_x$ and T-$Ni_{0.25}$/$Au_{1-x}Ag_x$. (c) DRS results of pristine TiO_2, T-$Ni_{0.25}$, T/$Au_{1-x}Ag_x$ and T-$Ni_{0.25}$/$Au_{1-x}Ag_x$ with (d) transformed plots based on the Kubelka–Munk function *vs.* energy of light. High-resolution (e) Ti 2p, (f) O 1s, (g) Ni 2p, (h) Au 4f and (i) Ag 3d spectra of (I) pristine TiO_2, (II) T-$Ni_{0.25}$ and (III) T-$Ni_{0.25}$/$Au_{1-x}Ag_x$.

capacity of TiO_2. The optical absorption edge of pristine TiO_2 is located in the ultraviolet light region of approximately 400 nm, corresponding to its intrinsic bandgap excitation.[17] According to the Kubelka–Munk function, the E_g value of TiO_2 is determined to be approximately 3.00 eV. For the composite samples, E_g values of T-$Ni_{0.25}$, T/$Au_{1-x}Ag_x$, and T-$Ni_{0.25}$/$Au_{1-x}Ag_x$ are determined to be 2.82 eV, 2.63 eV and 2.36 eV, respectively. Note that E_g decreases with Ni-doping and $Au_{1-x}Ag_x$ NC loading. Especially, T/$Au_{1-x}Ag_x$ and T-$Ni_{0.25}$/$Au_{1-x}Ag_x$ exhibit substantially improved visible-light absorption intensity after $Au_{1-x}Ag_x$ NC loading, primarily due to the photosensitization effect of $Au_{1-x}Ag_x$ NCs. In contrast, pure Ni-doping samples only marginally enhance the light absorption of TiO_2, implying that Ni acts as a co-catalyst rather than a light-harvesting component in the T-$Ni_{0.25}$/$Au_{1-x}Ag_x$ composite.

N_2 adsorption–desorption isotherms combined with Brunauer–Emmett–Teller (BET) and Barrett–Joyner–Halenda (BJH) analyses (Fig. S6 and Table S3) reveal the specific surface area and porosity of the samples. All the samples exhibit type IV isotherms and hysteresis loops at relative pressures (P/P_0) of 0.8–1.0, indicative of a mesoporous structure.[8] The BET specific surface areas of TiO_2, T-$Ni_{0.25}$, T/$Au_{1-x}Ag_x$, and T-$Ni_{0.25}$/$Au_{1-x}Ag_x$ are determined to be 86.63, 74.92, 42.95, and 40.51 $m^2\ g^{-1}$, respectively. The decreased surface area of TiO_2 with Ni and $Au_{1-x}Ag_x$ NC incorporation might stem from aggregation and pore filling, implying that the specific surface area does not contribute to the enhanced photoactivities of T/$Au_{1-x}Ag_x$, and T-$Ni_{0.25}$/$Au_{1-x}Ag_x$ heterostructures. Instead, atomic-scale dispersion of Ni in the oxide state and BNC deposition likely generate more surface reactive sites that are critical for charge transfer and catalytic activity.

X-ray photoelectron spectroscopy (XPS) was used to analyze the surface composition and chemical bond states of pristine TiO_2, T-$Ni_{0.25}$, T/$Au_{1-x}Ag_x$ and T-$Ni_{0.25}$/$Au_{1-x}Ag_x$ (Fig. S7 and Table S2). For pure TiO_2, the peaks of Ti 2p (Fig. 1e) at 458.6 and 464.4 eV correspond to the Ti^{4+} species, while the O 1 s signals at 529.9 eV and 531.5 eV are assigned to the lattice oxygen and adsorbed oxygen, respectively.[18] As for T-$Ni_{0.25}$, the obvious shifts in the Ti 2p and O 1s binding energies (Fig. 1e and f) relative to pure TiO_2 indicate the formation of strong Ni–O–Ti chemical bonds, confirming the covalent interaction between Ni species and the TiO_2 substrate. In contrast, T/$Au_{1-x}Ag_x$ displays no discernible shifts in the Ti 2p or O 1s signals compared with those of pure TiO_2 (Fig. S8), suggesting that $Au_{1-x}Ag_x$ NCs are physically adsorbed without disrupting the TiO_2 lattice. For T-$Ni_{0.25}$/$Au_{1-x}Ag_x$, the peak shifts are dominated by the Ni–TiO_2 interaction, while $Au_{1-x}Ag_x$ NCs are only adsorbed on the surface of the Ni-doped TiO_2 and do not destroy the interaction between Ni species and the TiO_2 substrate. The high-resolution Ni 2p spectrum of T-$Ni_{0.25}$/$Au_{1-x}Ag_x$ (Fig. 1g) displays the characteristic peaks of Ni^{2+} at 855.3 eV, 861.3 eV, 872.9 eV, and 878.3 eV.[19] The Au 4f signal of the T-$Ni_{0.25}$/$Au_{1-x}Ag_x$ heterostructure (Fig. 1h) reveals a mixture of metallic Au (0) (84.1 eV and 87.6 eV) and oxidized Au(I) (84.5 eV and 88.2 eV) for $Au_{1-x}Ag_x$ NCs, while the Ag 3d peaks at 367.9 eV and 374.0 eV (Fig. 1i) verify the presence of Ag(I) species,[2a] aligning with the BNC composition. The XPS results of T-$Ni_{0.25}$/$Au_{1-x}Cu_x$ and T-$Ni_{0.25}$/$Au_{1-x}Pt_x$ are specifically provided in Fig. S9 and S10, respectively. These XPS results confirm that Ni doping induces the atomic-scale interfacial bonding with TiO_2, facilitating the interfacial charge transfer, while $Au_{1-x}Ag_x$ NCs act as efficient visible-light absorbers through physical adsorption. The XPS results strongly substantiate the successful Ni ion doping and BNC decoration in the ternary heterostructure. Moreover, the lack of structural disruption by BNC deposition ensures the integrity of the Ni–TiO_2 interaction, thereby forming the synergistic heterostructure critical for enhanced photocatalytic performance.

As shown in Fig. 2a–f and S11, images at various magnifications reveal that all the samples maintain the two-dimensional (2D) nanosheet morphology of the TiO_2 substrate, suggesting that Ni doping and $Au_{1-x}Ag_x$ NC loading do not alter the underlying architecture. As displayed in Fig. 2b and c and S12, TEM and HRTEM images of pristine TiO_2 and T-$Ni_{0.25}$ exhibit a regular 2D nanosheet morphology with lateral dimensions of 20–60 nm and a lattice spacing of 0.35 nm, corresponding to the (101) crystal plane of anatase TiO_2.[8] Critically, no distinct Ni nanoparticles or aggregates are observable in the TEM images of T-$Ni_{0.25}$ (Fig. 2a–c), indicating that Ni is atomically dispersed or doped rather than forming bulk particles. In the TEM images of T-$Ni_{0.25}$/$Au_{1-x}Ag_x$ (Fig. 2d–f), $Au_{1-x}Ag_x$ NCs appear as ultra-small size entities with a size of about 2 nm or less, uniformly distributed across the TiO_2 nanosheets without disrupting the crystalline structure of the substrate.[20] This confirms that the electrostatic self-assembly process effectively anchors the $Au_{1-x}Ag_x$ NCs onto the Ni-doped TiO_2 nanosheet surface while preserving the nanosheet morphology. Energy-dispersive X-ray spectroscopy (EDS) mapping results (Fig. 2g–n) of the T-$Ni_{0.25}$/$Au_{1-x}Ag_x$ composite material show homogeneous distributions of Ti, O, Ni, Au, and Ag elements, corroborating the aforementioned XPS results and once again providing direct evidence for the successful incorporation of both Ni and $Au_{1-x}Ag_x$ NCs ingredients. The uniform dispersion of Ni dopants and $Au_{1-x}Ag_x$ NCs across the TiO_2 nanosheets underscores the structural integrity of the heterostructure. This morphological and compositional characterization collectively establishes that the synthetic strategy achieves atomic-level dispersion of Ni dopants while achieving ultrafine clustering of $Au_{1-x}Ag_x$ NCs on the TiO_2 nanosheets, forming a well-defined heterostructure critical for efficient charge separation and photocatalytic activity.

3.2 Photocatalytic H_2 generation activities

Using tri-ethanolamine (TEOA) as a hole-trapping agent, photocatalytic hydrogen evolution activities of the samples were systematically evaluated under visible light irradiation ($\lambda > 420$ nm). As shown in Fig. 3a, pristine TiO_2 exhibited no hydrogen production activity under visible light, attributed to its wide bandgap which precludes the band-gap-photoexcitation.[21] Upon Ni doping , the photocatalytic hydrogen evolution activity of T-$Ni_{0.25}$ remains undetectable, indicating that Ni doping alone cannot confer TiO_2 with visible-light responsiveness, which agrees with the DRS result. In contrast, T/10$Au_{1-x}Ag_x$, T-

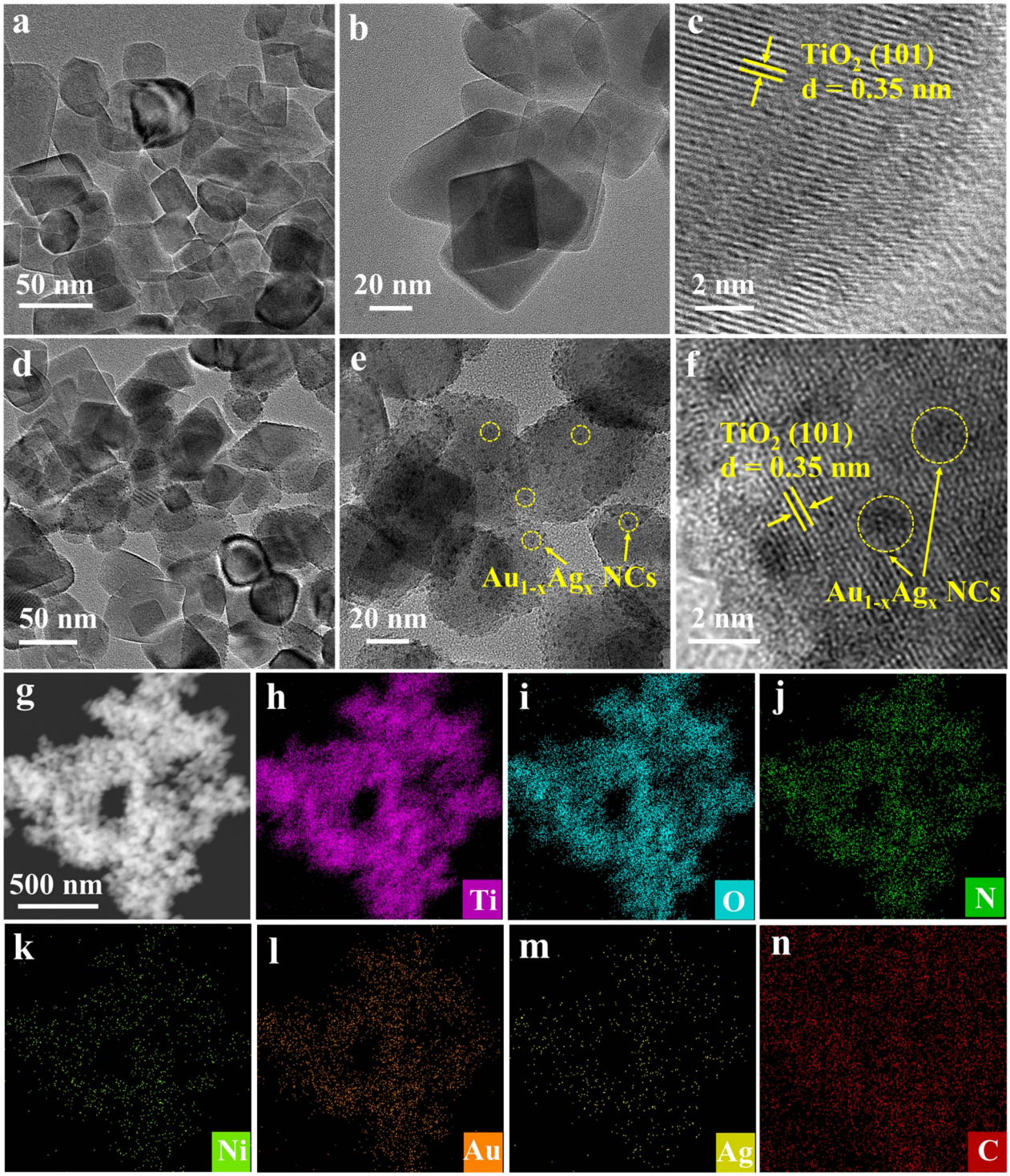

Fig. 2 TEM and HRTEM images of (a–c) T-$Ni_{0.25}$ and (d–f) T-$Ni_{0.25}/Au_{1-x}Ag_x$ with corresponding (g–n) elemental mapping results for (h) Ti, (i) O, (j) N, (k) Ni, (l) Au, (m) Ag, and (n) C signals.

$Ni_{0.46}/10Au_{1-x}Ag_x$, and T-$Ni_{0.25}/10Au_{1-x}Ag_x$ display measurable hydrogen production, implying that $Au_{1-x}Ag_x$ NCs act as efficient photosensitizers, extending the photo-response range of TiO_2 into the visible spectrum. The enhanced photocatalytic performance of T-$Ni_{0.46}/10Au_{1-x}Ag_x$ compared with T/$10Au_{1-x}Ag_x$ strongly highlights the critical role of Ni dopants as a co-catalyst in accelerating the interfacial electron transfer, thereby improving the charge separation efficiency.[9] Optimization of $Au_{1-x}Ag_x$ NC loading (Fig. 3b) revealed that T/$10Au_{1-x}Ag_x$ with 10 mL of BNCs exhibited the highest hydrogen evolution rate of 0.36 mmol g^{-1} h^{-1}, reflecting the optimal balance between light absorption and charge transport.[22] Further tuning of Ni doping

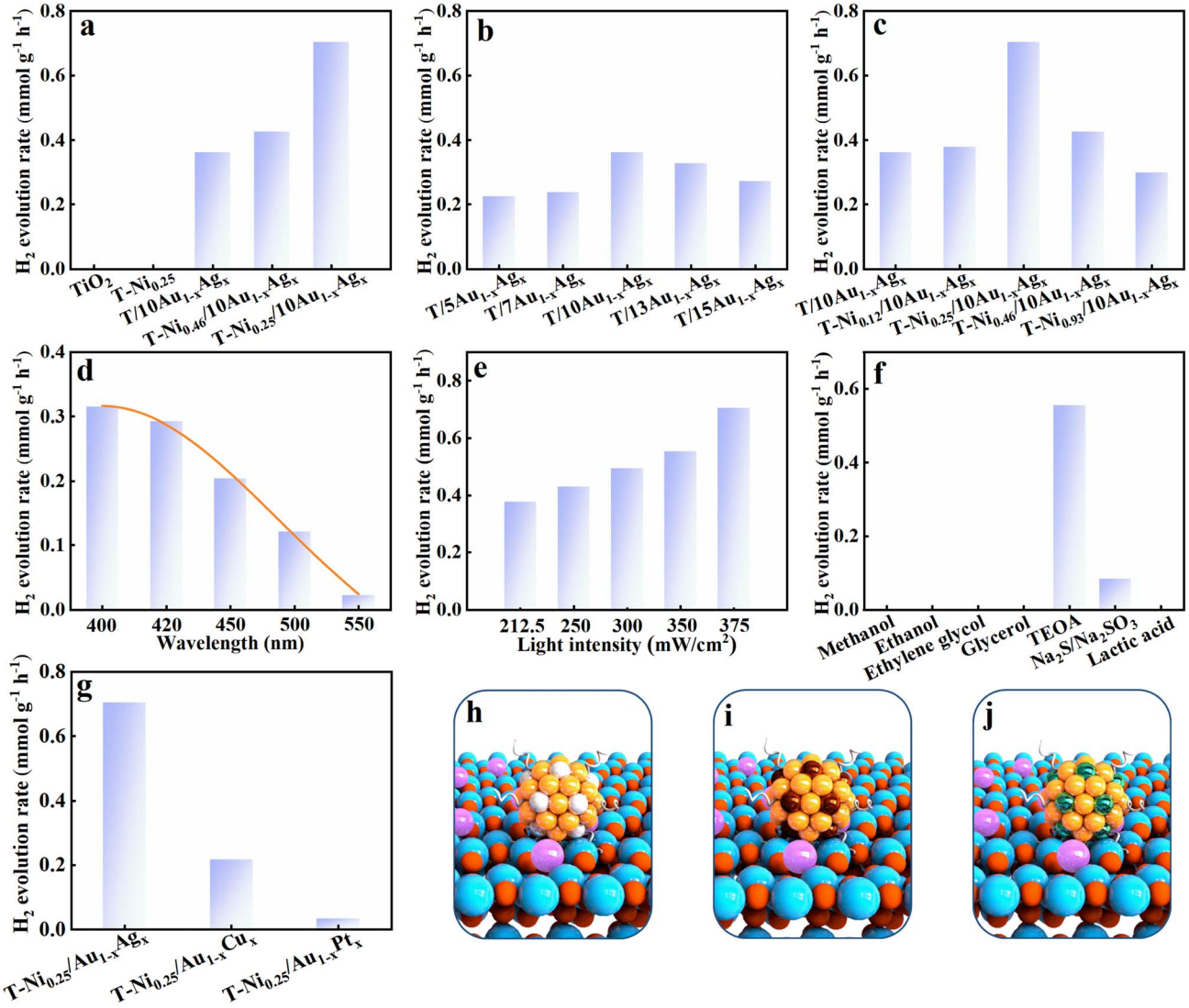

Fig. 3 (a) Photoactivity comparison among pristine TiO_2, T-$Ni_{0.25}$, T/$10Au_{1-x}Ag_x$, T-$Ni_{0.46}$/$10Au_{1-x}Ag_x$ and T-$Ni_{0.25}$/$10Au_{1-x}Ag_x$ toward hydrogen generation under visible light ($\lambda > 420$ nm) irradiation. Photocatalytic H_2 evolution performances of TiO_2–Ni/$Au_{1-x}Ag_x$ with different (b) $Au_{1-x}Ag_x$ and (c) Ni loading amounts under visible light ($\lambda > 420$ nm) irradiation. Photocatalytic H_2 evolution performances of T-$Ni_{0.25}$/$10Au_{1-x}Ag_x$ under (d) different monochromatic light irradiation wavelengths, (e) varying light intensities and (f) sacrificial reagents. (g) Photoactivity comparison among T-$Ni_{0.25}$/$AuAg_{10}$, T-$Ni_{0.25}$/$AuCu_{10}$, and T-$Ni_{0.25}$/$AuPt_{10}$. Schematic diagram depicting the structures of (h) TiO_2–$Ni_{0.25}$/$Au_{1-x}Ag_x$, (i) TiO_2–$Ni_{0.25}$/$Au_{1-x}Cu_x$ and (j) TiO_2–$Ni_{0.25}$/$Au_{1-x}Pt_x$.

levels (Fig. 3c) suggests that T-$Ni_{0.25}$/$10Au_{1-x}Ag_x$ containing 0.25 wt% Ni and 10 mL of $Au_{1-x}Ag_x$ NCs achieved a significantly higher hydrogen evolution rate of 0.70 mmol g^{-1} h^{-1}, establishing it as the optimal catalyst for subsequent systematic investigation.

Inductively coupled plasma-mass spectrometry (ICP-MS) was employed to quantitatively determine the actual amount of $Au_{1-x}Ag_x$ NCs and Ni dopant in the T-$Ni_{0.25}$/$10Au_{1-x}Ag_x$ heterostructure. As summarized in Table S4, the loading percentage of $Au_{1-x}Ag_x$ NCs and Ni dopant in the T-$Ni_{0.25}$/$10Au_{1-x}Ag_x$ was approximately 3.83 and 0.09 wt%, respectively. This result signifies that even a small amount of Ni dopant surprisingly yielded a substantial enhancement in photoactivity, underscoring the critical role of Ni dopants as co-catalysts in facilitating the interfacial electron transfer. Monochromatic light irradiation tests (Fig. 3d) revealed that the photocatalytic hydrogen evolution performance of T-$Ni_{0.25}$/$10Au_{1-x}Ag_x$ decreases with increasing wavelength in the visible range, with the highest activity observed under near-ultraviolet light (λ = 400–420 nm). This wavelength dependence aligns with the DRS results, confirming that while $Au_{1-x}Ag_x$ NCs broaden the light absorption of TiO_2, the absorption efficiency remains primarily confined to the short-wavelength visible region. Light intensity measurements (Fig. 3e) show a linear increase in the photocatalytic hydrogen production rate with increasing light intensity, indicating that the photoreaction system operates under photon-limited conditions and possesses untapped potential for enhanced performance under

higher irradiance, verifying it is indeed a photocatalytic reaction. Photocatalytic experiments using different sacrificial agents (Fig. 3f) demonstrate that TEOA outperformed other hole scavengers (methanol, ethanol, ethylene glycol, glycerol, lactic acid, and Na_2S/Na_2SO_3), yielding the highest hydrogen evolution activity. This superiority is attributed to the suitable redox potential and strong hole-trapping ability of TEOA, facilitated by its tertiary amine group, which efficiently scavenges photogenerated holes and promotes sustained electron transfer to the catalyst surface, ultimately boosting the hydrogen generation.[23] The chemical structure and redox properties of the sacrificial agent are critical determinants of catalytic performance, underscoring the importance of system-wide optimization in photocatalytic hydrogen production. As displayed in Fig. S13, cyclic stability tests indicate that photoactivity of the T-$Ni_{0.25}$/10$Au_{1-x}Ag_x$ heterostructure exhibits apparent decay after the 2nd cycle. The relatively unfavorable cycling performance of the T-$Ni_{0.25}$/10$Au_{1-x}Ag_x$ heterostructure is likely attributed to the vigorous stirring during continuous photocatalytic reactions, which causes the detachment of $Au_{1-x}Ag_x$ NCs from the TiO_2 substrate, thereby weakening the visible-light absorption capacity of the composite and diminishing the number of active sites available for catalysis. More importantly, the intrinsically poor stability of metal NCs cannot be ignored, which leads to the gradual *in situ* transformation of metal NCs to conventional metal nanocrystals under continuous light irradiation, hence losing the advantageous photosensitization effect of metal NCs. Nevertheless, the significant enhancement in photocatalytic performance implies that the synergistic combination of $Au_{1-x}Ag_x$ NCs as photosensitizers and Ni dopants as a co-catalyst enables efficient visible-light-driven hydrogen evolution by expanding the spectral response of TiO_2 and optimizing charge carrier dynamics. To further assess the generality of this strategy, a series of other alloy NC-based T-$Ni_{0.25}$/[$Au_{1-x}Cu_x$, $Au_{1-x}Pt_x$] heterostructures were prepared using analogous methodologies for visible-light-driven photocatalytic hydrogen production. The related characterization of T-$Ni_{0.25}$/[$Au_{1-x}Cu_x$, $Au_{1-x}Pt_x$] heterostructures is specifically provided in Fig. S9 and S10. As shown in Fig. 3g, the T-$Ni_{0.25}$/$Au_{1-x}Ag_x$ heterostructure consistently exhibits the highest photoactivity among the tested systems under visible-light irradiation. Notably, all these alloy NC-modified samples (Fig. 3h–j) extend the light absorption spectrum of the TiO_2 substrate into the visible region and demonstrate measurable photocatalytic activities, collectively highlighting the universal applicability of $Au_{1-x}Ag_x$, $Au_{1-x}Cu_x$, and $Au_{1-x}Pt_x$ NCs as photosensitizers in this heterostructure design.

3.3 PEC and spectroscopic analysis

To elucidate the impact of BNC deposition and Ni doping on the interfacial charge separation efficiency of the T-$Ni_{0.25}$/$Au_{1-x}Ag_x$ artificial photosystem, a comprehensive set of photoelectrochemical (PEC) analyses were performed on each photocatalyst. Transient photocurrent response is regarded as the most intuitive method for evaluating the carrier separation efficiency of photoelectrodes.[24] Fig. 4a shows the periodic on/off transient photocurrent responses of pristine TiO_2, T-$Ni_{0.25}$, T/$Au_{1-x}Ag_x$, and the T-$Ni_{0.25}$/$Au_{1-x}Ag_x$ heterostructure under intermittent visible light irradiation ($\lambda > 420$ nm). Notably, the photocurrent density of T-$Ni_{0.25}$/$Au_{1-x}Ag_x$ is significantly higher than that of pristine TiO_2. Careful observation reveals that since TiO_2 is a wide bandgap semiconductor, it cannot be photoexcited under visible light, and thus it generates almost no photocurrent. Moreover, after the introduction of the Ni co-catalyst, the increase in the photocurrent density of T-$Ni_{0.25}$ is still relatively small since Ni doping fails to alter the light absorption of the TiO_2 substrate, as unveiled by the DRS result. However, after loading the $Au_{1-x}Ag_x$ NCs, both T/$Au_{1-x}Ag_x$ and T-$Ni_{0.25}$/$Au_{1-x}Ag_x$ generate apparent photocurrents under visible light, which strongly indicates that $Au_{1-x}Ag_x$ NCs serve as effective photosensitizers. The improved photocurrent of T-$Ni_{0.25}$/$Au_{1-x}Ag_x$ compared with that of T/$Au_{1-x}Ag_x$ indicates that Ni doping can indeed accelerate the interfacial electron transport, thereby enhancing the carrier separation efficiency, which is consistent with the aforementioned photocatalytic performance analysis. To explore the charge recombination dynamics, open-circuit photovoltage decay (OCVD) results of the photoanodes were studied, which is regarded as an effective tool to monitor the open-circuit voltage (V_{oc}) decay when the light is turned off in a stable state.[25] As shown in Fig. 4b, TiO_2 and T-$Ni_{0.25}$ show almost no voltage attenuation owing to their large bandgaps and negligible visible light absorption, while T-$Ni_{0.25}$/$Au_{1-x}Ag_x$ exhibits the maximum photovoltage, which once again confirms that the simultaneous introduction of $Au_{1-x}Ag_x$ and Ni doping leads to the most enhanced charge separation. Similarly, this result is fully consistent with the transient photocurrent response. Alternatively, Fig. 4c and Table S5 show the electrochemical impedance spectroscopy (EIS) results of the different samples under visible light irradiation. Among them, T-$Ni_{0.25}$/$Au_{1-x}Ag_x$ shows the minimum semi-circular arc radius, indicating that $Au_{1-x}Ag_x$ NC loading and Ni doping effectively reduce the interfacial charge transfer resistance of the heterostructure. Therefore, the PEC results strongly validate that the significant improvement in the photoactivity of T-$Ni_{0.25}$/$Au_{1-x}Ag_x$ is primarily attributed to the synergistic promotion of charge separation and migration afforded by Ni doping and $Au_{1-x}Ag_x$ NC photosensitization. According to the M–S results of TiO_2, T-$Ni_{0.25}$, T/$Au_{1-x}Ag_x$ and T-$Ni_{0.25}$/$Au_{1-x}Ag_x$ (Fig. S14), T-$Ni_{0.25}$/$Au_{1-x}Ag_x$ exhibits the largest charge carrier density (3.5×10^{19} cm^{-3}), confirming the key role of Ni doping and $Au_{1-x}Ag_x$ decoration in accelerating the interfacial charge separation. Overall, the results of photocurrent, OCVD, EIS, M–S and N_D analyses are consistent with the photocatalytic performances. In addition, according to the UV-Vis absorption spectra (Fig. S1e) and cyclic voltammetry (CV) results (Fig. S15), the highest occupied molecular orbital (HOMO) and the lowest unoccupied molecular orbital (LUMO) levels of $Au_{1-x}Ag_x$ NCs are determined to be approximately −2.235 V and 0.655 V *vs.* NHE (Fig. S18a), respectively. The HOMO and LUMO levels of $Au_{1-x}Cu_x$ and $Au_{1-x}Pt_x$ NCs were also determined by analogous methods (Fig. S16–S18).

To elucidate the photocatalytic mechanism, charge transport processes in TiO_2, T-$Ni_{0.25}$, T/$Au_{1-x}Ag_x$ and T-$Ni_{0.25}$/$Au_{1-x}Ag_x$

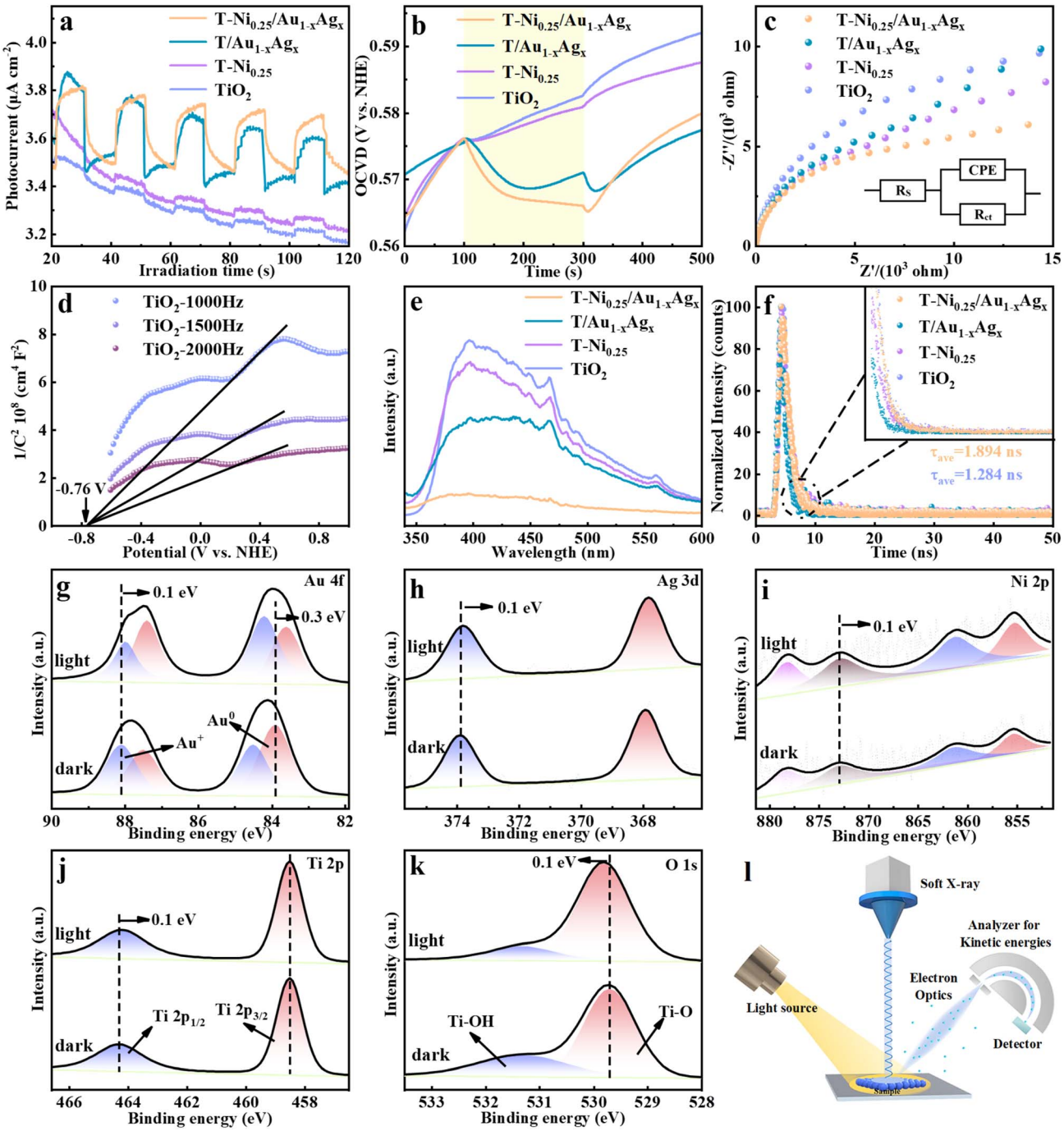

Fig. 4 (a) Photocurrents, (b) open-circuit voltage decay (OCVD), and (c) EIS Nyquist plots of pristine TiO_2, T-$Ni_{0.25}$, T/$Au_{1-x}Ag_x$ and T-$Ni_{0.25}$/$Au_{1-x}Ag_x$ under visible light (λ > 420 nm) irradiation, for which aqueous Na_2SO_4 solution (0.5 M, pH = 6.69) was utilized as the electrolyte. (d) Mott–Schottky plots of TiO_2 under different frequencies. (e) PL spectra and (f) time-resolved transient PL decay of pristine TiO_2, T-$Ni_{0.25}$, T/$Au_{1-x}Ag_x$ and T-$Ni_{0.25}$/$Au_{1-x}Ag_x$. *In situ* irradiated XPS high-resolution (g) Au 4f, (h) Ag 3d, (i) Ni 2p, (j) Ti 2p and (k) O 1s spectra of T-$Ni_{0.25}$/$Au_{1-x}Ag_x$ with and without light irradiation (λ > 420 nm). (l) Schematic diagram of *in situ* irradiated XPS for probing high-resolution spectra.

were studied spectroscopically. Photoluminescence (PL) spectroscopy was employed to analyze the carrier recombination efficiency. As shown in Fig. 4e, steady-state PL spectra of the samples were recorded under 360 nm excitation. All the composite samples exhibit lower PL intensities compared with pure TiO_2, indicating that Ni doping and $Au_{1-x}Ag_x$ NC photosensitization significantly suppress the electron–hole pair recombination. Among them, T-$Ni_{0.25}$/$Au_{1-x}Ag_x$ shows the lowest PL intensity, signifying its maximally suppressed carrier recombination and optimal charge separation. Time-resolved photoluminescence (TRPL) decay curve spectroscopy was used to probe the carrier dynamics of the photosystems. The fitting

results (Fig. 4f and Table S6) reveal that the average lifetime of the optimal sample T-$Ni_{0.25}/Au_{1-x}Ag_x$ is 1.894 ns, compared with 1.598 ns for pristine TiO_2. The extended average lifetime of T-$Ni_{0.25}/Au_{1-x}Ag_x$ indicates a reduction in radiative recombination, suggesting an increased availability of carriers for the photocatalytic reaction. These results collectively demonstrate that concurrent Ni doping and $Au_{1-x}Ag_x$ NC loading synergistically inhibit the carrier recombination. Comparative analysis of the photoactivities, PEC performances and PL results (Fig. 4a–f) between T/$Au_{1-x}Ag_x$ and T-$Ni_{0.25}/Au_{1-x}Ag_x$ further confirms that Ni doping enhances the overall performances of the samples. We speculate that the Ni dopant acts as an efficient electron transfer mediator, facilitating the unidirectional and smooth electron flow from $Au_{1-x}Ag_x$ NCs to the TiO_2 substrate, thereby validating its role as a co-catalyst.

In situ XPS characterization, a powerful technique to analyze the surface chemistry and charge transport mechanisms of photocatalysts, was also performed.[26] The changes in the binding energies of core elements directly reflect the variation in electron density. As illustrated in Fig. 4g–i, obvious shifts in the binding energies of Au 4f, Ag 3d, and Ni 2p for the T-$Ni_{0.25}/Au_{1-x}Ag_x$ composite were observed under visible light irradiation compared with the dark-state conditions. These shifts verify the occurrence of photoelectron transfer upon light exposure, providing crucial evidence for determining the charge transfer pathways of the composite materials under visible light irradiation. Specifically, as TiO_2 is inactive under visible light, photoelectrons generated in the $Au_{1-x}Ag_x$ NCs migrate to the TiO_2 substrate, and the Ni dopant functioning as a co-catalyst accelerates the electron migration process. This is rationalized by the blue-shift in the binding energies of Ti 2p and O 1s for the T-$Ni_{0.25}/Au_{1-x}Ag_x$ heterostructure (Fig. 4j–k). Noteworthily, the reduced binding energy of Ni 2p for the T-$Ni_{0.25}/Au_{1-x}Ag_x$ heterostructure upon light irradiation also indicates the electron flow from $Au_{1-x}Ag_x$ NCs to the Ni dopant that acts as an interfacial electron transport mediator (Fig. 4i).

3.4 Photocatalytic mechanism

To deeply investigate the photogenerated charge separation behavior, Kelvin probe force microscopy (KPFM) was employed to obtain high-resolution nanoscale images of surface morphology and potential. KPFM operates based on the work function difference between the probe and the sample.[27] Upon contact, electron flow equilibrates their Fermi levels, producing a contact potential difference (CPD) that depends on both the probe work function (Φ_t) and the sample work function (Φ_s), as shown in Fig. 5e.[28] Thus, variations in CPD directly reveal the distribution and separation of charge carriers on the sample surface.[29] Fig. S20 & Fig. 5 present the surface morphologies and potential images of all the samples. As shown in Fig. 5a1–d1, pristine TiO_2, T-$Ni_{0.25}$, T/$Au_{1-x}Ag_x$ and T-$Ni_{0.25}/Au_{1-x}Ag_x$ exhibit non-uniform potential distribution across the scanned region, and differences in CPD before and after visible light irradiation (Fig. 5a2–d2) are clearly visible through color contrast in the potential maps. Under visible light illumination conditions, photogenerated electron–hole pairs separate, leading to an increase in CPD for all the samples. The corresponding ΔCPD values for pure TiO_2, T-$Ni_{0.25}$, T/$Au_{1-x}Ag_x$ and T-$Ni_{0.25}/Au_{1-x}Ag_x$ are determined to be 9 mV, 10.7 mV, 28.2 mV, and 74 mV, respectively (Fig. 5a3d–3 and a4–d4). The positive ΔCPD indicates greater hole accumulation on the surface after light illumination, meaning the surface potential change is primarily governed by holes.[30] Comparisons reveal that the ΔCPD changes of pure TiO_2 and T-$Ni_{0.25}$ are relatively small. In contrast, after depositing $Au_{1-x}Ag_x$ NCs, both T/$Au_{1-x}Ag_x$ and T-$Ni_{0.25}/Au_{1-x}Ag_x$ exhibit significantly enhanced ΔCPD, with the latter showing the most pronounced increase. This suggests that T-$Ni_{0.25}/Au_{1-x}Ag_x$ accumulates more photogenerated charges on the surface under visible light illumination.[31] Additionally, the CPD line–scan profiles (Fig. S21a4–d4) further verify this trend, that is, T-$Ni_{0.25}/Au_{1-x}Ag_x$ displays the largest CPD enhancement, strongly confirming its more efficient directional exciton transfer and improved spatial separation of electron–hole pairs. These findings align with the PEC results, jointly confirming the superior photogenerated charge separation and transfer capability of the T-$Ni_{0.25}/Au_{1-x}Ag_x$ heterostructure.

Elucidating the modulation of the electronic structure and atomic coordination environment of the doped Ni species in TiO_2 is crucial for understanding the photocatalytic mechanism of the T-$Ni_{0.25}/Au_{1-x}Ag_x$ heterostructure. Density functional theory (DFT) calculations were performed to determine the preferential location of Ni species in the TiO_2 substrate. As shown in Fig. 6a, the configuration where Ni adsorbs on the TiO_2 surface, forming direct Ni–O bonds, yields a binding energy of −4.20 eV. In contrast, the substitution of Ni at Ti sites in the TiO_2 bulk results in a binding energy of only −0.05 eV. The significantly more negative binding energy for surface adsorption indicates that this configuration is energetically far more favorable. This computational conclusion is consistent with the EXAFS results below, which suggest the formation of Ni–O bonds on the TiO_2 surface rather than replacement of Ti atoms with Ni.

The Ni doping of TiO_2 by the MSM method, enabled by high-temperature conditions, facilitates Ni–O bond formation between freely mobile Ni^{2+} ions and surface oxygen ions of TiO_2, as corroborated by extended X-ray absorption fine structure (EXAFS) and X-ray absorption near-edge structure (XANES) spectroscopy (Fig. 6a and b). As shown in Fig, 6b, the absorption edge of TiO_2–Ni is positioned closer to that of NiO than to metallic Ni foil, indicating that the valence state of Ni in TiO_2–Ni lies between +1 and +2, closely approaching the +2 state.[32] Ni K-edge R-space EXAFS analysis (Fig, 6c) of TiO_2–Ni reveals two characteristic peaks at 1.6 Å and 2.6 Å which are analogous to those of NiO, corresponding to the Ni–O and Ni–Ni coordinate ion bonds, respectively.[33] As shown in Table S7, the fitting results of the EXAFS data are specifically summarized. Notably, the absence of the Ni–Ni bonding peak of metallic Ni foil within the TiO_2–Ni spectrum indicates that Ni species are dispersed rather than forming metallic atoms, strongly suggesting their existence in an oxidized state.[34] Additionally, wavelet transform (WT) analysis of the EXAFS spectra was performed to verify the atomic dispersion (Fig. 6e–g). In comparison with the WT profiles of Ni foil and NiO, TiO_2–Ni exhibits two obvious

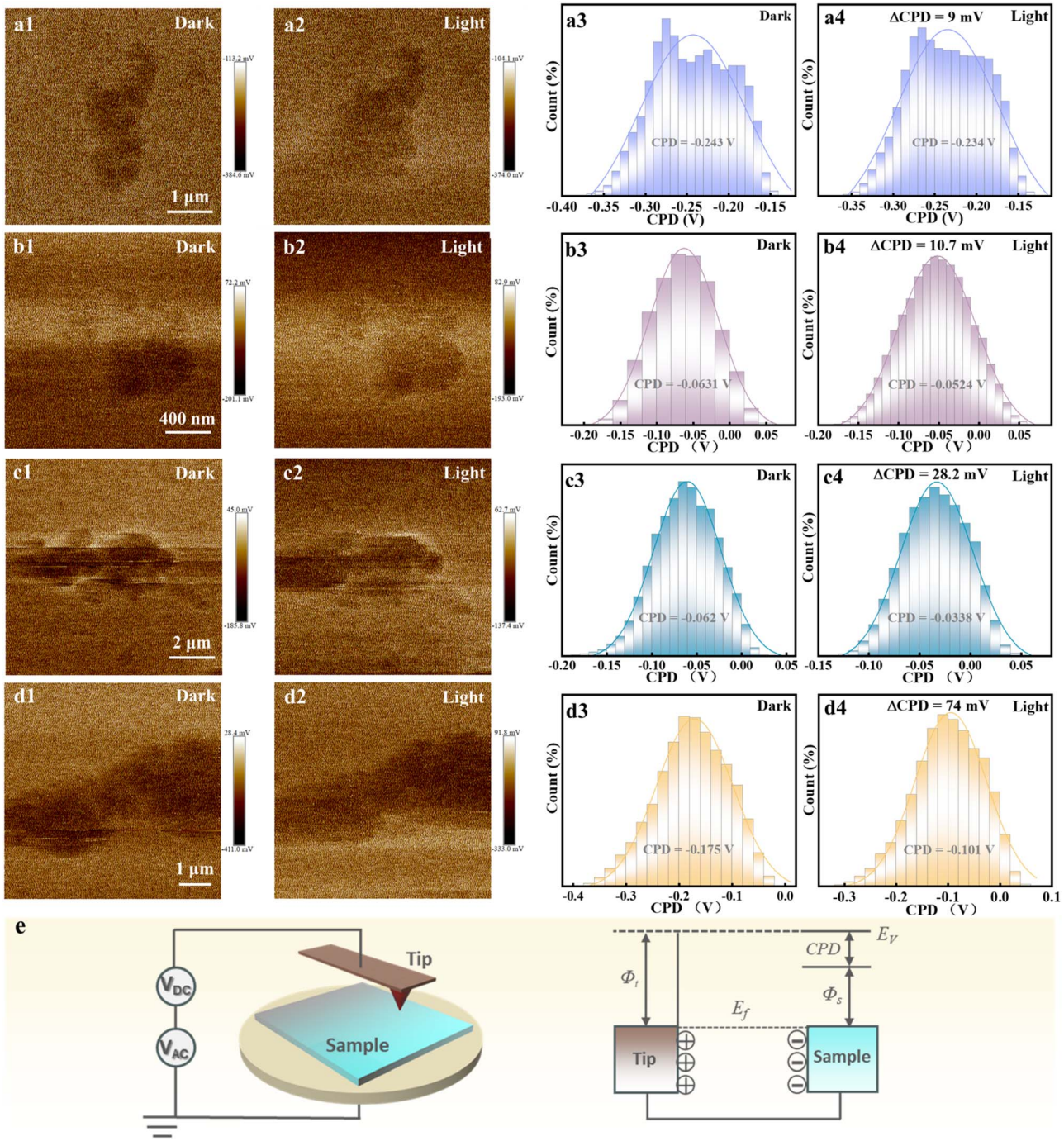

Fig. 5 KPFM images of (a) pristine TiO_2, (b) T-$Ni_{0.25}$, (c) T/$Au_{1-x}Ag_x$ and (d) T-$Ni_{0.25}$/$Au_{1-x}Ag_x$ (a1–d1) under dark conditions and (a2–d2) under visible light irradiation. Corresponding surface contact potential distributions (CPDs) of pristine TiO_2, T-$Ni_{0.25}$, T/$Au_{1-x}Ag_x$ and T-$Ni_{0.25}$/$Au_{1-x}Ag_x$ (a3–d3) under dark conditions and (a4-d4) under visible light irradiation. (e) Schematic illustration of CPD determination by KPFM measurement on the sample surface.

coordination signals at approximately 5 $Å^{-1}$ and 9 $Å^{-1}$, corresponding to Ni–O and Ni–Ni coordination, respectively. This indicates that the Ni species on TiO_2–Ni are in an oxidized state, which is consistent with the EXAFS results. Collectively, these results provide unambiguous evidence for the successful doping of Ni onto the TiO_2 surface, with the formation of Ni–O surface linkages critical for modulating the electronic structure of the semiconductor.

Based on the M–S results (Fig. 4d), the conduction band (CB) potential (E_{CB}) of TiO_2 was determined to be −0.76 V relative to NHE (−0.34 V relative to RHE), and considering that the E_{fb} of an n-type semiconductor is more positive by 0.1 V than the E_{CB}, E_{CB} of TiO_2 is calibrated to be −0.86 V *vs.* NHE. Given that the bandgap of TiO_2 determined from the DRS results is 3.00 eV (Fig. 1d), the valence band (VB) level of TiO_2 is thus calculated to be 2.14 eV relative to NHE. Based on the experimental analyses,

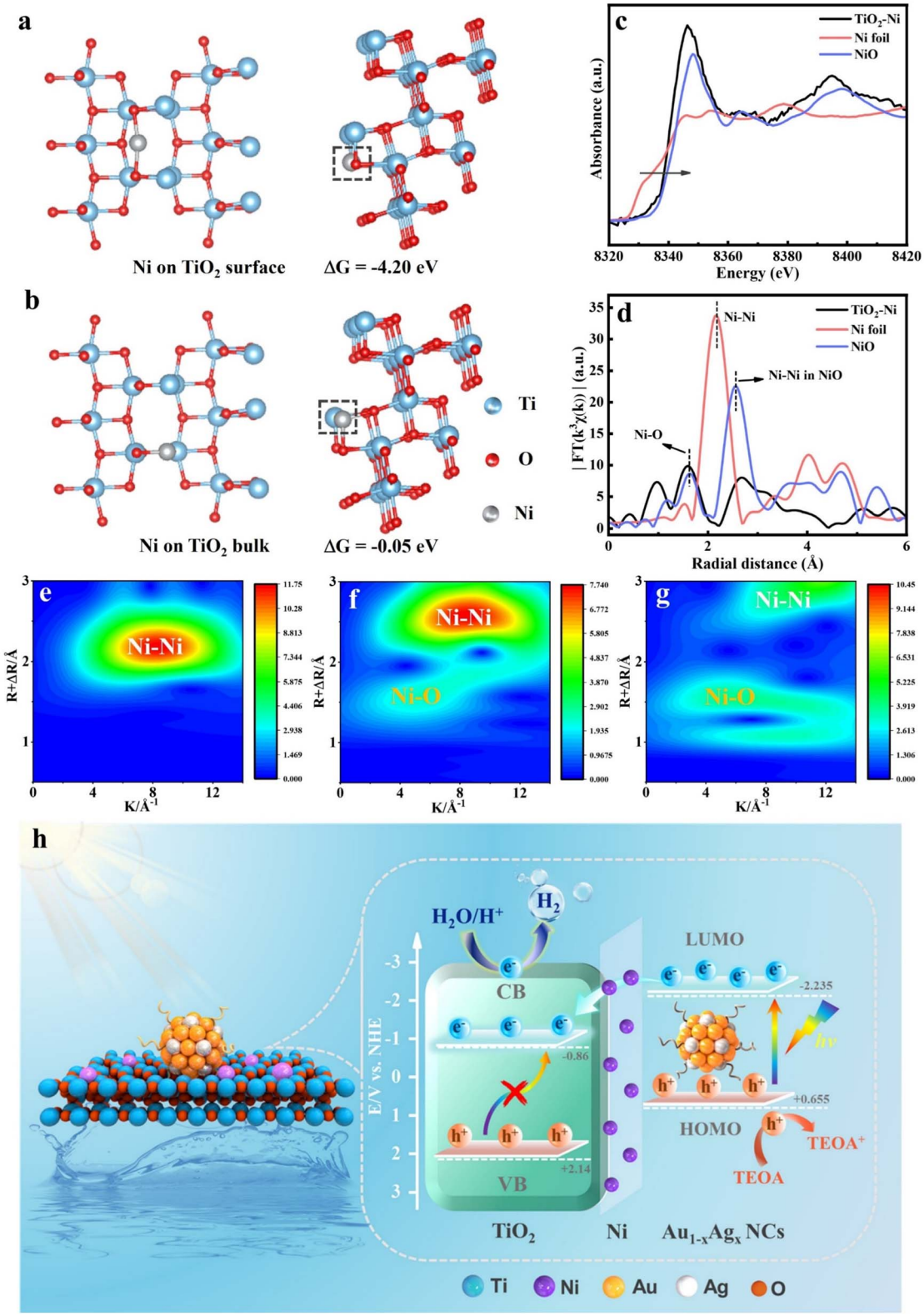

Fig. 6 The molecular models of Ni (a) on the surface and (b) in the bulk of TiO_2. (c) XANES and (d) EXAFS spectra of TiO_2–Ni. Wavelet transform (WT) for the EXAFS signals of (e) Ni foil, (f) NiO and (g) TiO_2–Ni. (h) Schematic illustration of the photocatalytic mechanism of the T-$Ni_{0.25}$/$Au_{1-x}Ag_x$ heterostructure.

a photocatalytic mechanism is proposed, as illustrated in Fig. 6h. When the T-$Ni_{0.25}/Au_{1-x}Ag_x$ heterostructure is irradiated with visible light, $Au_{1-x}Ag_x$ NCs undergo photoexcitation, inducing electron transitions from the HOMO to the LUMO level. Owing to the favorable energy level alignment between the LUMO level of $Au_{1-x}Ag_x$ NCs and the CB of TiO_2, photoexcited electrons in the LUMO level of $Au_{1-x}Ag_x$ NCs rapidly inject into the CB of the TiO_2 substrate, establishing a direct charge transfer pathway. The Ni species doped on the TiO_2 surface function as a co-catalyst *via* strong Ni–O chemical bonding which plays a dual role by lowering the energy barrier for electron transfer from $Au_{1-x}Ag_x$ NCs to TiO_2 through modulating the interfacial electronic structure and constructing a cascaded electron transport pathway, thereby accelerating the directional charge migration. This Ni-mediated synergy significantly suppresses the electron–hole recombination and enhances the separation efficiency of photogenerated charge carriers over $Au_{1-x}Ag_x$ NCs.[9,35] Subsequently, the transferred electrons accumulate at the TiO_2 surface and then react with protons (H^+) adsorbed at the active sites on the TiO_2 surface to drive the hydrogen evolution reaction. The discrete energy levels of BNCs combined with the uniform dispersion of Ni co-catalysts, create a robust "light absorption–charge separation–proton reduction" cascade charge transfer channel, enabling efficient conversion of solar energy into chemical energy. The synergy between molecular-like BNCs as light-harvesting units and Ni co-catalysts as charge-accelerating nodes represents a rational design strategy for constructing high-performance heterostructure photocatalysts, providing a foundational framework for advancing solar-to-hydrogen conversion technologies.

The TiO_2–Ni/alloy NCs demonstrate a more superior photocatalytic mechanism compared to traditional semiconductor photocatalysts and metal nanoparticles. Conventional semiconductor photocatalysts generate electron–hole pairs *via* interband transitions but are often constrained by limited visible-light response and rapid carrier recombination.[36] Metal nanoparticles can contribute *via* plasmonic effects or hot-electron injection, yet their function is typically confined to isolated steps.[37] In contrast, metal NCs possess a discrete electronic structure with both molecule-like and nanomaterial-like characteristics, enabling more versatile light absorption and charge transfer pathways. Furthermore, BNCs allow compositional tuning to optimize energy-level alignment with the semiconductor. In this work, BNCs form a favorable cascade alignment with TiO_2–Ni, promoting efficient electron transition, suppressing charge recombination, and prolonging excited-state carrier lifetimes.

4. Conclusions

To sum up, TiO_2–Ni/alloy NC ($Au_{1-x}Ag_x$, $Au_{1-x}Pt_x$, and $Au_{1-x}Cu_x$) heterostructures were fabricated by a facile and universal molten salt method combined with an electrostatic self-assembly strategy. The results confirm that BNC ($Au_{1-x}Ag_x$, $Au_{1-x}Pt_x$, and $Au_{1-x}Cu_x$) decoration extends the light absorption of TiO_2 into the visible region; meanwhile Ni doping accelerates the interfacial charge transport, thus synergistically boosting the electron separation from BNCs to TiO_2. This synergy significantly enhances the visible-light-driven photocatalytic hydrogen evolution performances of TiO_2–Ni/alloy NC ($Au_{1-x}Ag_x$, $Au_{1-x}Pt_x$, and $Au_{1-x}Cu_x$) heterostructures by virtue of their favorable energy level alignment. Furthermore, the charge transfer mechanism of TiO_2–Ni/alloy NC artificial photosystems was unraveled, revealing a synergistic effect between atomic-scale metal NCs and metal oxide supports.

Author contributions

Zi-Han Zheng performed the experiments, analyzed all the data, and drafted the manuscript. Qing Chen and Peng Su carried out and analyzed a portion of the experiments. Fang-Xing Xiao guided this work and corrected the manuscript. Lifeng Cai, Jie Liang, and Guangcan Xiao helped to check the manuscript. All the authors contributed to critical discussion of the data and the manuscript.

Conflicts of interest

The authors declare no competing interests.

Data availability

All data supporting the findings of this study are available within the paper and its supplementary information (SI) files. Source data are provided with this paper. Supplementary information is available. See DOI: https://doi.org/10.1039/d6sc02262f.

Acknowledgements

The support from the Award Program for Minjiang scholar professorship is greatly acknowledged. This work was financially supported by the National Natural Science Foundation of China (No. 21703038 and 22072025). The financial support from the State Key Laboratory of Structural Chemistry, Fujian Institute of Research on the Structure of Matter, Chinese Academy of Sciences (No. 20240018), and the Natural Science Foundation of Fujian Province (2024J01263) is acknowledged.

References

1 (*a*) R. C. Jin, C. J. Zeng, M. Zhou and Y. X. Chen, *Chem. Rev.*, 2016, **116**, 10346–13413; (*b*) I. Chakraborty and T. Pradeep, *Chem. Rev.*, 2017, **117**, 8208–8271; (*c*) X. Kang, Y. W. Li, M. Z. Zhu and R. C. Jin, *Chem. Soc. Rev.*, 2020, **49**, 6443–6514; (*d*) L. C. Liu and A. Corma, *Chem. Rev.*, 2018, **118**, 4981–5079; (*e*) Y. X. Du, H. T. Sheng, D. Astruc and M. Z. Zhu, *Chem. Rev.*, 2020, **120**, 526–622.

2 (*a*) Q. L. Mo, B. J. Liu and F. X. Xiao, *J. Phys. Chem. C*, 2021, **125**, 22421–22428; (*b*) L. P. Zhang, J. R. Ran, S. Z. Qiao and M. Jaroniec, *Chem. Soc. Rev.*, 2019, **48**, 5184–5206.

3 (*a*) X. Y. Fu, Z. Q. Wei, S. Xu, X. Lin, S. Hou and F. X. Xiao, *J. Phys. Chem. Lett.*, 2020, **11**, 9138–9143; (*b*) H. Liang, B. J. Liu, B. Tang, S. C. Zhu, S. Li, X. Z. Ge, J. L. Li, J. R. Zhu and

F. X. Xiao, *ACS Catal.*, 2022, **12**, 4216–4226; (*c*) H. Wang, F. Chen, W. Li and T. Tian, *J. Power Sources*, 2015, **287**, 150–157.

4 (*a*) Y. Z. Bao, X. H. Wu, H. J. Gao, M. M. Zhou, S. Chen, S. Jin, H. Z. Yu and M. Z. Zhu, *Dalton Trans.*, 2020, **49**, 17164–17168; (*b*) Y. Du, Z. J. Guan, Z. R. Wen, Y. M. Lin and Q. M. Wang, *Chem. - Eur. J.*, 2018, **24**, 16029–16035; (*c*) A. G. Walsh and P. Zhang, *J. Phys. Chem. Lett.*, 2021, **12**, 257–275; (*d*) X. Q. Ren, X. M. Fu, X. Z. Lin, J. Tang, H. Wang, C. Liu and J. H. Huang, *Eur. J. Inorg. Chem.*, 2021, **2021**, 2281–2283; (*e*) X. Kang and M. Z. Zhu, *Small*, 2019, **15**, e1902703; (*f*) C. Zhu, Z. L. Chen, H. Li, L. Y. Lu, X. Kang, J. Xuan and M. Z. Zhu, *J. Am. Chem. Soc.*, 2024, **146**, 23212–23220; (*g*) M. Kamachi, K. Yonesato, T. Okazaki, D. Yanai, S. Kikkawa, S. Yamazoe, R. Ishikawa, N. Shibata, Y. Ikuhara, K. Yamaguchi and K. Suzuki, *Angew. Chem., Int. Ed.*, 2024, **63**, e202408358; (*h*) X. J. Zou, S. P. He, X. Kang, S. Chen, H. Z. Yu, S. Jin, D. Astruc and M. Z. Zhu, *Chem. Sci.*, 2021, **12**, 3660–3667; (*i*) E. H. Kim, M. H. Lee, J. Kim, E. C. Ra, J. H. Lee and J. S. Lee, *Chin. J. Catal.*, 2023, **47**, 214–221.

5 (*a*) L. Ji, D. Spanu, N. Denisov, S. Recchia, P. Schmuki and M. Altomare, *Chem.–Asian J.*, 2020, **15**, 301–309; (*b*) Z. H. N. Al-Azri, W.-T. Chen, A. Chan, V. Jovic, T. Ina, H. Idriss and G. I. N. Waterhouse, *J. Catal.*, 2015, **329**, 355–367; (*c*) Y. Liu, Y. Li, F. Peng, Y. Lin, S. Yang, S. Zhang, H. Wang, Y. Cao and H. Yu, *Appl. Catal. B Environ.*, 2019, **241**, 236–245.

6 (*a*) R. Shen, J. Xie, Q. Xiang, X. Chen, J. Jiang and X. Li, *Chin. J. Catal.*, 2019, **40**, 240–288; (*b*) S. M. Thabet, H. N. Abdelhamid, S. A. Ibrahim and H. M. El-Bery, *Sci. Rep.*, 2024, **14**, 10115; (*c*) J. S. Schubert, J. Popovic, G. M. Haselmann, S. P. Nandan, J. Wang, A. Giesriegl, A. S. Cherevan and D. Eder, *J. Mater. Chem. A*, 2019, **7**, 18568–18579; (*d*) P. D. Tran, L. Xi, S. K. Batabyal, L. H. Wong, J. Barber and J. S. Chye Loo, *Phys. Chem. Chem. Phys.*, 2012, **14**, 11596–11599; (*e*) X. Zhao, W. Xie, X. Shao, Z. Wang, B. Yang, C. Yang, J. Wang and X. Su, *Mater. Sci. Semicond. Process.*, 2022, **148**, 106775.

7 (*a*) M. A. Nazir, T. Najam, M. Altaf, K. Ahmad, I. Hossain, M. A. Assiri, M. S. Javed, A. u. Rehman and S. S. A. Shah, *J. Alloys Compd.*, 2024, **990**, 174378; (*b*) Z. Fu, X. Ma, B. Xia, X. Hu, J. Fan and E. Liu, *Int. J. Hydrogen Energy*, 2021, **46**, 19373–19384; (*c*) M. Zhai, Z. Li, R. Li, Z. Feng, Q. Wang, C. Zhang, H. Chi, N. Ta and C. Li, *J. Catal.*, 2025, **443**, 115989; (*d*) J. J. Zhao, P. F. Liu, Y. L. Wang, Y. H. Li, M. Y. Zu, C. W. Wang, X. L. Wang, L. J. Fang, H. D. Zeng and H. G. Yang, *Chem. - Eur. J.*, 2017, **23**, 16734–16737; (*e*) J. Zhang, Z. Yu, Z. Gao, H. Ge, S. Zhao, C. Chen, S. Chen, X. Tong, M. Wang, Z. Zheng and Y. Qin, *Angew. Chem., Int. Ed.*, 2016, **56**, 816–820.

8 J. Shen, C. Luo, S. Qiao, Y. Chen, K. Fu, J. Xu, J. Pei, Y. Tang, X. Zhang, H. Tang, H. Zhang and C. Liu, *Adv. Funct. Mater.*, 2023, **34**, 2309056.

9 M. Xiao, L. Zhang, B. Luo, M. Lyu, Z. Wang, H. Huang, S. Wang, A. Du and L. Wang, *Angew. Chem., Int. Ed.*, 2020, **59**, 7230–7234.

10 D. Hikosou, S. Saita, S. Miyata, H. Miyaji, T. Furuike, H. Tamura and H. Kawasaki, *J. Phys. Chem. C*, 2018, **122**, 12494–12501.

11 X. Liu, N. Fechler and M. Antonietti, *Chem. Soc. Rev.*, 2013, **42**, 8237–8265.

12 (*a*) J. Ryu, J. H. Seo, G. Song, K. Choi, D. Hong, C. Wang, H. Lee, J. H. Lee and S. Park, *Nat. Commun.*, 2019, **10**, 2351; (*b*) Y. Yuan, W. Xiao, Z. Wang, D. J. Fray and X. Jin, *Angew. Chem., Int. Ed.*, 2018, **57**, 15743–15748.

13 (*a*) J. P. Holmberg, E. Ahlberg, J. Bergenholtz, M. Hassellöv and Z. Abbas, *J. Colloid Interface Sci.*, 2013, **407**, 168–176; (*b*) A. M. Jastrzębska, P. Kurtycz, A. Olszyna, E. Karwowska, E. Miaśkiewicz-Pęska, M. Załęska-Radziwiłł, N. Doskocz and D. Basiak, *Int. J. Appl. Ceram. Technol.*, 2014, **12**, 1157–1173.

14 (*a*) L. Yang, X. Jiang, W. Ruan, B. Zhao, W. Xu and J. R. Lombardi, *J. Phys. Chem. C*, 2008, **112**, 20095–20098; (*b*) X. Li, Y. Wu, Y. Shen, Y. Sun, Y. Yang and A. Xie, *Appl. Surf. Sci.*, 2018, **427**, 739–744.

15 Z. Y. Li, Y. H. Chen, J. R. Zhu, Q. Chen, S. J. Lu and F. X. Xiao, *Inorg. Chem.*, 2023, **62**, 16965–16973.

16 K. Kuroi, M. Yamada, I. Kawamura, M. Jung, C.-G. Pack and F. Fujii, *Phys. Chem. Chem. Phys.*, 2022, **24**, 13356–13364.

17 A. Li, S. Chen, F. Yang, H. Gao, C. Dong and G. Wang, *Inorg. Chem.*, 2021, **60**, 18337–18346.

18 (*a*) H. Zhuang, W. Chen, W. Xu and X. Liu, *Int. J. Energy Res.*, 2020, **44**, 3224–3230; (*b*) Y. Yang, X. Li, C. Lu and W. Huang, *Catal. Lett.*, 2019, **149**, 2930–2939.

19 (*a*) L. Ma, R. Guan, W. Kang, Z. Sun, H. Li, Q. Li, Q. Shen, C. Chen, X. Liu, H. Jia and J. Xue, *J. Colloid Interface Sci.*, 2024, **660**, 381–392; (*b*) X. Shi, L. Mao, C. Dai, P. Yang, J. Zhang, F. Dong, L. Zheng, M. Fujitsuka and H. Zheng, *J. Mater. Chem. A*, 2020, **8**, 13376–13384.

20 G. Wu, Q. L. Mo, Y. Xiao, K. Wang, X. Z. Ge, S. R. Xu, J. L. Li, Y. Q. Shao and F. X. Xiao, *Inorg. Chem.*, 2023, **62**, 520–529.

21 Y. Wang, X. H. Liu, Q. Wang, M. Quick, S. A. Kovalenko, Q. Y. Chen, N. Koch and N. Pinna, *Angew. Chem., Int. Ed.*, 2020, **59**, 7748–7754.

22 K. Wang, X.-Z. Ge, Q.-L. Mo, X. Yan, Y. Xiao, G. Wu, S.-R. Xu, J.-L. Li, Z.-X. Chen and F.-X. Xiao, *J. Catal.*, 2022, **416**, 92–102.

23 (*a*) G. Malekshoar and A. K. Ray, *Chem. Eng. Sci.*, 2016, **152**, 35–44; (*b*) W. Jones, D. J. Martin, A. Caravaca, A. M. Beale, M. Bowker, T. Maschmeyer, G. Hartley and A. Masters, *Appl. Catal. B Environ.*, 2019, **240**, 373–379.

24 J.-N. Yuan, X. Yan, B.-X. Zheng, J.-Q. Chen and F.-X. Xiao, *Inorg. Chem. Front.*, 2025, **12**, 1553–1567.

25 P. Su, S. Li and F. X. Xiao, *Small*, 2024, **20**, 2400958.

26 L. Wang, Y. Li, Y. Ai, E. Fan, F. Zhang, W. Zhang, G. Shao and P. Zhang, *Adv. Funct. Mater.*, 2023, **33**, 2306466.

27 W. Melitz, J. Shen, A. C. Kummel and S. Lee, *Surf. Sci. Rep.*, 2011, **66**, 1–27.

28 (*a*) J. Cheng, S. Wan and S. Cao, *Angew. Chem., Int. Ed.*, 2023, **62**, e202310476; (*b*) J. Cheng, W. Wang, J. Zhang, S. Wan, B. Cheng, J. Yu and S. Cao, *Angew. Chem., Int. Ed.*, 2024, **63**, e202406310.

29 R. Li, H. Li, X. Zhang, B. Liu, B. Wu, B. Zhu, J. Yu, G. Liu, L. Zheng and Q. Zeng, *Adv. Funct. Mater.*, 2024, **34**, 2402797.

30 (*a*) C. Cheng, B. He, J. Fan, B. Cheng, S. Cao and J. Yu, *Adv. Mater.*, 2021, **33**, 2100317; (*b*) X. Zhang, J. Xu, H. Long, J. Yu and H. Yu, *ACS Catal.*, 2024, **14**, 18669–18678.

31 (*a*) C. Yang, S. Wan, B. Zhu, J. Yu and S. Cao, *Angew. Chem., Int. Ed.*, 2022, **61**, e202208438; (*b*) Y. Tang, Z.-F. Xu, Y. Sun, C. Wang, Y. Guo, W. Hao, X. Tan, J. Ye and T. Yu, *Energy Environ. Sci.*, 2024, **17**, 7882–7894.

32 (*a*) W. Zhong, C. Yang, J. Wu, W. Xu, R. Zhao, H. Xiang, K. Shen, Q. Zhang and X. Li, *Chem. Eng. J.*, 2022, **436**, 134813; (*b*) T. Chen, F. Wang, S. Cao, Y. Bai, S. Zheng, W. Li, S. Zhang, S. X. Hu and H. Pang, *Adv. Mater.*, 2022, **34**, 2201779.

33 M. Liu, Y. Ji, Y. Li, P. An, J. Zhang, J. Yan and S. Liu, *Small*, 2021, **17**, 2102448.

34 B. He, P. Xiao, S. Wan, J. Zhang, T. Chen, L. Zhang and J. Yu, *Angew. Chem., Int. Ed.*, 2023, **62**, e202313172.

35 J. Yang, Z. Qiu, C. Zhao, W. Wei, W. Chen, Z. Li, Y. Qu, J. Dong, J. Luo, Z. Li and Y. Wu, *Angew. Chem., Int. Ed.*, 2018, **57**, 14095–14100.

36 (*a*) J. Deng, X. Xu, B. Su, M. Liu, X. Lin, W. Xing, X. F. Lu, Z. Lan, G. Zhang and S. Wang, *Mater. Horiz.*, 2025, **12**, 5702–5709; (*b*) Z. Wang, B. Su, J. Xu, Y. Hou and Z. Ding, *Int. J. Hydrogen Energy*, 2020, **45**, 4113–4121.

37 (*a*) S. Sarina, H.-Y. Zhu, Q. Xiao, E. Jaatinen, J. Jia, Y. Huang, Z. Zheng and H. Wu, *Angew. Chem., Int. Ed.*, 2014, **53**, 2935–2940; (*b*) B. Su, K. Tang, J. Cai, X. Lin, W. Xing, K. Liu, X. F. Lu, Y. Hou, W.-J. Ong and S. Wang, *ACS Catal.*, 2026, **16**, 5208–5217.